Nuclear Science and Techniques (2025) 36:156
https://doi.org/10.1007/s41365-025-01755-8

Coherent Compton scattering using a stretched off-axis paraboloid

Kai Zhao[1] · **Chang-Bo Fu**[1] · **Xiang-Jin Kong**[1] · **Yu-Gang Ma**[1]

Received: 6 January 2025 / Revised: 14 February 2025 / Accepted: 23 February 2025 / Published online: 26 June 2025

Abstract
Extreme ultraviolet (EUV) lithography is crucial for advancing semiconductor manufacturing; however, current EUV light sources, such as laser-produced plasma (LPP), have significant limitations, including low energy-conversion efficiency and debris contamination. Various schemes, including optical free-electron laser undulators, have been studied to generate coherent EUV light. However, optical undulators suffer from limited focal lengths, which pose a significant challenge to achieving a higher gain. In this study, a novel approach is proposed that employs a stretched off-axis paraboloid (sOAP) mirror, thus extending the focus distance to the centimeter range while achieving a well-controlled periodic light field. This enables high-intensity 92-eV EUV sources to exceed 10^{16}/s, as demonstrated in the simulations. The proposed setup provides an efficient and powerful solution for advanced applications including semiconductor lithography.

Keywords Laser Compton scattering (LCS) · Coherent scattering · Free-electron laser (FEL)

1 Introduction

As chip manufacturers strive to produce increasingly smaller and more powerful devices, extreme ultraviolet (EUV) lithography has become essential in the industry [1–4]. EUV light enables the creation of intricately small patterns on silicon wafers, which form the basis for integrated circuits. Currently, EUV lithography relies predominantly on laser-produced plasma (LPP) as the light source [5]. Although LPP serves as a basis for sub-5 nm node production, it has several limitations that hinder its further advancement. These include an extremely low energy-conversion efficiency, with less than 1% of the laser energy being transformed into usable EUV radiation, and tin debris contamination of optical components, which imposes a cost burden owing to frequent cleaning or replacement [2].

Plans for next-generation coherent EUV sources based on free-electron laser (FEL) technologies are being developed to replace current incoherent LPP-based systems. For example, KEK has proposed an energy recovery linac free-electron laser (ERL-FEL) system [6]. Operating at a frequency of 162.5 MHz with an average current of 10 mA, this system provides EUV radiation at a wavelength of 13.5 nm with an output power greater than 10 kW. Based on the superconducting synchrotron microbunching (SSMB) concept, Tsinghua University, along with Pohang (Korea) and other institutions, is developing EUV sources [7–9]. These proposals rely on magnetic undulators. However, other approaches that do not depend on magnetic undulators are also in development.

FELs that use optical undulators have been proposed for many years [10]; however, progress has been limited. One of the main challenges is the insufficient gain length [11]. A key issue with optical undulators is that focusing is often used to increase the light intensity, which reduces the gain length. However, if loose focusing is used to increase the interaction region between the electrons and photons (thus increasing the gain length), the light intensity decreases. This dilemma can be addressed using the flying focus method [12–14]. In this approach, the light field is modulated and sequentially focused at different spatial positions over time. Essentially,

---

This work was supported in part by the National Key R&D Program of China (No. 2023YFA1606900) and the National Natural Science Foundation of China (NSFC) (Nos. 12235003 and 12447106).

✉ Chang-Bo Fu
cbfu@fudan.edu.cn

✉ Yu-Gang Ma
mayugang@fudan.edu.cn

[1] Key Laboratory of Nuclear Physics and Ion-beam Application (MOE), Institute of Modern Physics, Fudan University, Shanghai 200433, China

at any given moment, the focus is at a small spatial region, and at the next moment, the focus shifts to another region, as if the focus flies across the space. This dynamic focusing technique allows the beam to maintain its intensity while significantly increasing its gain length [15].

The flying focus technique can achieve a focus distance of several centimeters [11] compared with the traditional focus distance of several tens of micrometers, significantly improving the gain length without sacrificing light intensity. This breakthrough can help overcome one of the major limitations of optical undulators in FELs. It has been estimated that an EUV source with an output power of up to 1 MW can be achieved using this approach [11], marking a major advancement in the development of high-power EUV sources for applications such as semiconductor lithography.

However, generating a flying focus remains a challenge. Various approaches have been proposed, including the use of Kerr lenses [16]. However, the nonlinear properties of Kerr lenses can lead to instability. Recently, axiparabolas have been used in high-intensity laser plasma applications and to generate flying foci [17–20]. In this study, the use of a specialized axiparabola, stretched off-axis paraboloid (sOAP), is investigated to produce coherent EUV light through Compton scattering. Instead of a conventional flying focus, a structured flying focus or flying focus train can be generated using a sOAP.

In the following sections, the optical properties of the sOAP and the theory of coherent Compton scattering are first described. Next, the proposed setup utilizing a tilted pulse laser, sOAP, and flying focus train is introduced. Finally, the EUV light yield of the proposed configuration is evaluated.

2 Stretched off-axis paraboloid mirror

The proposed sOAP mirror, as shown in Fig. 1, satisfies the following equation in cylindrical coordinates (r, θ, z):

$$z = \frac{r^2}{4f_0(1+\eta z/f_0)} \simeq \frac{r^2}{4f_0}(1-\eta z/f_0), \tag{1}$$

where f_0 represents the major focal length, and η is a tunable parameter $|\eta| \ll 1$. If $\eta < 0$, the off-axis paraboloid (OAP) is compressed. However, for simplicity, it is still referred to as a sOAP.

Without a loss of generality, $\theta = 0$ is set in the following discussion to restrict attention to the 2D case (r, z).

2.1 Focus location

Rewriting Eq. 1 obtains the following:

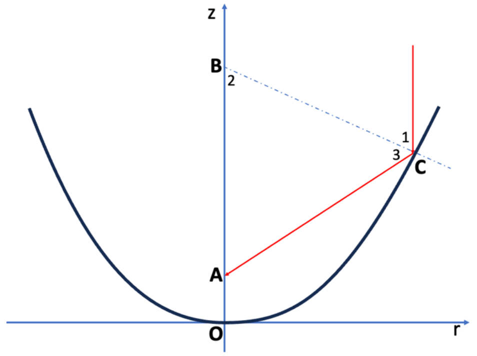

Fig. 1 (Color online) Sketch of a sOAP, as defined by Eq. 1. The incoming beam strikes at point **C**, where it is reflected toward point **A**, located on the axis. Point **B** represents the normal direction of the tangent surface at point **C**

$$z^2 + \frac{f_0}{\eta}z - \frac{1}{4\eta}r^2 = 0. \tag{2}$$

From this equation, the coordinates of the incident point C of the ray shown in Fig. 1 is deduced as follows:

$$C = \left(r, \frac{f_0}{2\eta}\left[\sqrt{1+\frac{r^2}{f_0^2}\eta} - 1\right]\right). \tag{3}$$

In the limit of $\eta \to 0$, the coordinates are simplified as follows:

$$C = \left(r, \frac{r^2}{4f_0}\left[1 - \frac{r^2}{4f_0^2}\eta\right]\right). \tag{4}$$

The slope of the tangent at point C is as follows:

$$\frac{\mathrm{d}z}{\mathrm{d}r} = \frac{r}{2f_0\left(1+\frac{2\eta z}{f_0}\right)}. \tag{5}$$

Using this, the equation for the normal line passing from point C is derived as follows:

$$Y = -\frac{2f_0\left(1+\frac{2\eta z}{f_0}\right)}{r}X + \frac{r^2}{4f_0}\left(1-\frac{r^2}{4f_0^2}\eta\right) + 2f_0\left(1+\frac{2\eta z}{f_0}\right). \tag{6}$$

The coordinates of the point B are approximately:

$$B \simeq \left(0, \frac{r^2}{4f_0}\left[1-\frac{r^2}{4f_0^2}\eta\right] + 2f_0\left[1+\frac{\eta r^2}{2f_0^2}\right]\right). \tag{7}$$

As $\angle 1 = \angle 3$ and $\angle 1 = \angle 2$, it is deduced that $\angle 2 = \angle 3$, which implies that $BA = AC$.

The length AC is given by:

$$AC^2 = r^2 + \left[\frac{r^2}{4f_0}\left(1 - \frac{r^2}{4f_0^2}\eta\right) - OA \right]^2. \tag{8}$$

The focal length $f = OA$ is r-dependent. From the relationship $OA = OB - BA = OB - AC$, it follows that:

$$f = A_1 + A_2 - \sqrt{r^2 + \left(A_1 - f\right)^2}, \tag{9}$$

where:

$$A_1 = \frac{r^2}{4f_0}\left(1 - \frac{r^2}{4f_0^2}\eta\right), \quad A_2 = 2f_0\left(1 + \frac{r^2}{2f_0^2}\eta\right). \tag{10}$$

Thus:

$$f = A_1 + \frac{A_2}{2} - \frac{r^2}{2A_2}. \tag{11}$$

Retaining only the first-order terms in η, the following is obtained:

$$f \simeq f_0\left[1 + \left(\frac{r^4}{16f_0^4} + \frac{r^2}{2f_0^2}\right)\eta\right]. \tag{12}$$

Taking $z \simeq r^2/4f_0$, the following is obtained:

$$f \simeq f_0\left[1 + \left(\frac{z^2}{f_0^2} + \frac{2z}{f_0}\right)\eta\right]. \tag{13}$$

As $\eta \to 0$, $f = f_0$ becomes constant, which is a characteristic of a normal OAP.

2.2 Focus speed

The optical path difference is expressed as $\Delta_{\text{laser}} = \Delta(AC) - \Delta z$ (Fig. 1). The value of Δ_{laser} is determined as follows:

Considering Eq. 8 and substituting Eq. 12 while retaining only the first-order terms of η, the following is obtained:

$$\begin{aligned} AC^2 &\simeq f_0^2 + \frac{r^2}{2} + \frac{r^4}{16f_0^2} + r^2\eta - \frac{r^6\eta}{16f_0^4} \\ &= \left(f_0 + \frac{r^2}{4f_0}\right)^2 + \left(r^2 - \frac{r^6}{16f_0^4}\right)\eta. \end{aligned} \tag{14}$$

Thus:

$$\begin{aligned} AC &\simeq f_0 + \frac{r^2}{4f_0} + \frac{r^2 - \frac{r^6}{16f_0^4}}{2(f_0 + \frac{r^2}{4f_0})}\eta \\ &= f_0 + \frac{r^2}{4f_0} + \frac{r^2}{2f_0^2}\left(1 - \frac{r^2}{4f_0^2}\right)\eta f_0. \end{aligned} \tag{15}$$

This leads to the following:

$$\frac{\mathrm{d}(AC)}{\mathrm{d}r} \simeq \frac{r}{2f_0} + \frac{\eta r}{f_0} - \frac{\eta r^3}{2f_0^3}. \tag{16}$$

From Eq. 1, the following is obtained:

$$\frac{\mathrm{d}z}{\mathrm{d}r} \simeq \frac{r}{2f_0}\left(1 - \frac{r^2\eta}{2f_0^2}\right). \tag{17}$$

Combining Eqs. 16 and 17, the following is obtained:

$$\frac{\mathrm{d}(AC - z)}{\mathrm{d}r} \simeq \frac{\eta r}{f_0} - \frac{\eta r^3}{4f_0^3}. \tag{18}$$

Taking the derivative of Eq. 12, the following is obtained:

$$\frac{\mathrm{d}f}{\mathrm{d}r} \simeq \frac{r^3\eta}{4f_0^3} + \frac{r\eta}{f_0}. \tag{19}$$

Combining Eqs. 19 and 18, the following is obtained:

$$\frac{\mathrm{d}(AC - z)}{\mathrm{d}f} \simeq \frac{\frac{\eta r}{f_0} - \frac{\eta r^3}{4f_0^3}}{\frac{r^3\eta}{4f_0^3} + \frac{r\eta}{f_0}}. \tag{20}$$

Let $v_{\text{f}} \equiv \mathrm{d}f/\mathrm{d}t$, and given that $\mathrm{d}(AC - z)/\mathrm{d}t = c$ where c is the speed of light, it follows that:

$$v_{\text{f}} = \frac{1 + \frac{r^2}{4f_0^2}}{1 - \frac{r^2}{4f_0^2}}c = \frac{1 + z/f_0}{1 - z/f_0}c. \tag{21}$$

It can be observed that v_{f}, the speed of the focal points, is always greater than the speed of light. This is because the speed referred to here does not correspond to the motion of any physical object or the photons themselves. Moreover, because all light rays considered here travel in a vacuum, Fermat's principle of least time forbids the two focal points from being connected in time.

According to Eq. 21, in both cases where $r \gg f_0$ (Fig. 2a) and $r \ll f_0$ (Fig. 2c), $|v_{\text{f}}| \simeq c$. In the case where $r^2 = 4f_0^2$ (Fig. 2b), $v_{\text{f}} \to \infty$. By setting $\mathrm{sgn}(\eta)$, v_{f} is adjusted along or against the beam direction.

2.3 Beam phase in the focus line

The relationship between the optical path difference ΔL and phase difference $\Delta\phi$ can be expressed as follows:

$$\Delta\phi = \frac{2\pi}{\lambda}\Delta L,$$

where λ is the wavelength of the light.

Inserting this into Eq. (20), the following is obtained:

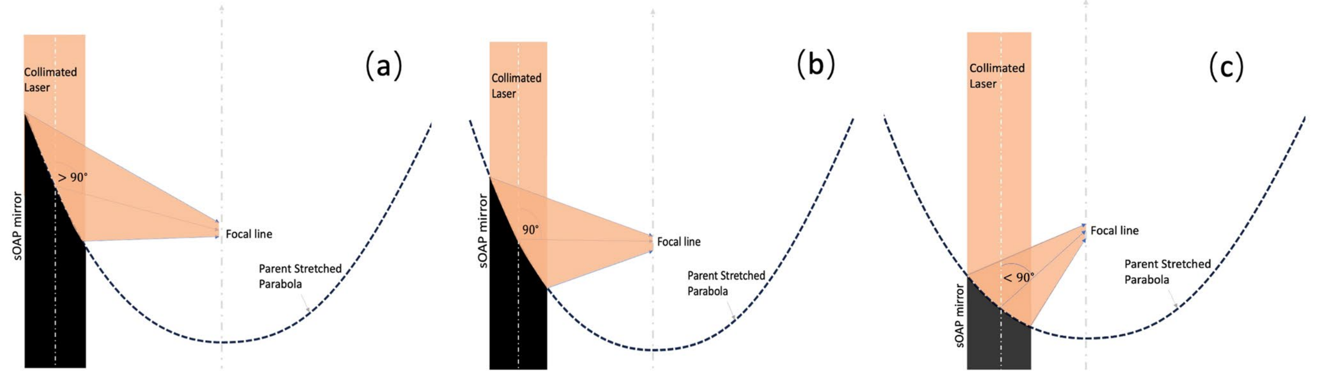

Fig. 2 (Color online) Three configurations of the sOAP are considered: The beam is focused at angles > 90° (**a**), = 90° (**b**), and < 90° (**c**). The sOAP mirror is a segment of the parent stretched parabola described by Eq. 1. Due to the stretching, the beam is focused into a line rather than a single point, as would be the case with a standard OAP

$$\frac{\mathrm{d}\phi}{\mathrm{d}f}=\frac{2\pi}{\lambda}\frac{(1-z/f_0)}{(1+z/f_0)}. \tag{22}$$

For the case where $z \simeq f_0$, which means that the off-axis angle is approximately 90° along the z-direction, the wave number is approximately:

$$k_\mathrm{w} \equiv \frac{\mathrm{d}\phi}{\mathrm{d}f} \simeq 0. \tag{23}$$

For the cases where $z \ll f_0$ and $z \gg f_0$, it follows that:

$$k_\mathrm{w} \simeq \pm\frac{2\pi}{\lambda}. \tag{24}$$

2.4 Focus length

As shown in Eq. 13, instead of focusing on a single point as in a normal OAP, the sOAP focuses on a line of length L_f:

$$\begin{aligned} L_\mathrm{f} =& f_\mathrm{max} - f_\mathrm{min} \\ =& (z_\mathrm{max} - z_\mathrm{min})\eta\left[\frac{z_\mathrm{max}+z_\mathrm{min}}{f_0}+2\right] \\ =& 2\Delta z\,\eta\left(\frac{\bar{z}}{f_0}+1\right). \end{aligned} \tag{25}$$

where f_max and f_min refer to the focal lengths at positions z_max and z_min, respectively; $\bar{z} \equiv (z_\mathrm{max} + z_\mathrm{min})/2$ and $\Delta z \equiv z_\mathrm{max} - z_\mathrm{min}$. The focal length is related to the mirror size in the z-direction as well as the parameter η.

Note that the requirement is $|\eta| \ll 1$, but it is not necessary for η to remain constant. Thus, $\eta \propto \eta_0 \sin(k_t z)$ is set, where $\eta_0 \ll 1$ is a constant and the beam intensity $I(z)$ along the focal length is modulated as $I(z) \propto \eta_0 \sin^2(k_t z)$.

3 Coherent compton scattering

Consider the scattering of a bunch of electrons with a spatial distribution $\rho_\mathrm{e}(\mathbf{r})$, and a bunch of photons with a spatial distribution $\rho_\ell(\mathbf{r})$. The momenta of the electrons before and after the interaction are $\mathbf{k}_\mathrm{e}$ and $\mathbf{k}'_\mathrm{e}$, respectively, and momentum transfer is defined as $\mathbf{q} = \mathbf{k} - \mathbf{k}'$. In the impulse approximation, the total amplitude of the scattered photon wave function $\mathbf{A}_{\ell'}(\mathbf{R})$ far away from the scattering area is given by:

$$\mathbf{A}_{\ell',t}(\mathbf{R}) = \bar{\mathbf{A}}_\ell(\mathbf{R})F(\mathbf{q}), \tag{26}$$

where $\bar{\mathbf{A}}_\ell$ denotes the average amplitude of a single photon scattered by a single electron, $|\mathbf{R}|$ is significantly larger than the size where photons and electrons exist, and $F(\mathbf{q})$ is the *double form factor* of the distributions of the electrons and photons defined as [21, 22]:

$$F(\mathbf{q}) = \iint \rho_\mathrm{e}(\mathbf{r}_\mathrm{e})\rho_\ell(\mathbf{r}_\ell)e^{i\mathbf{q}\cdot(\mathbf{r}_\mathrm{e}-\mathbf{r}_\ell)}\mathrm{d}\mathbf{r}_\mathrm{e}\mathrm{d}\mathbf{r}_\ell, \tag{27}$$

where ρ_e (ρ_ℓ) represents the electron (photon) density of the bunch. The *double form factor* $F(\mathbf{q})$ characterizes the spatial distribution of the electrons and photons as a Fourier transform of $\rho_\mathrm{e}(\mathbf{r}_\mathrm{e})\rho_\ell(\mathbf{r}_\ell)$. The intensity of scattered radiation ($I_{\ell'}$) is proportional to $|\mathbf{A}_{\ell',t}|^2$.

Thus, coherent Compton scattering can be achieved in two ways. The first option is to reduce the interaction area between electrons and photons, that is, $|\mathbf{r}_\mathrm{e} - \mathbf{r}_\ell| \ll 1/|\mathbf{q}|$. In this case, according to Eq. 27, the integral is simplified as follows: $F(\mathbf{q}) \approx \iint \rho_\mathrm{e}(\mathbf{r}_\mathrm{e})\rho_\ell(\mathbf{r}_\ell)\mathrm{d}\mathbf{r}_\mathrm{e}\mathrm{d}\mathbf{r}_\ell = \mathcal{N}_\mathrm{e}\mathcal{N}_\ell$, where $\mathcal{N}_\mathrm{e} = \int \rho_\mathrm{e}(\mathbf{r}_\mathrm{e})\mathrm{d}\mathbf{r}_\mathrm{e}$ and $\mathcal{N}_\ell = \int \rho_\ell(\mathbf{r}_\ell)\mathrm{d}\mathbf{r}_\ell$ are the total numbers of electrons and photons, respectively, leading to coherent scattering, where the scattered intensity scales as follows:

$$I_{\ell'} \propto |\mathbf{A}_{\ell',t}|^2 \propto \mathcal{N}_e^2 \mathcal{N}_{\ell}^2. \tag{28}$$

However, if $|\mathbf{r}_e - \mathbf{r}_{\ell}| \ll 1/|\mathbf{q}|$ is not satisfied, when the momentum transfer $\mathbf{q}$ increases, $e^{i\mathbf{q}\cdot(\mathbf{r}_e - \mathbf{r}_{\ell})}$ induces a destructive interference. Consequently, $F(\mathbf{q})$ approaches zero, which indicates incoherent scattering. The requirement that $|\mathbf{r}_e - \mathbf{r}_{\ell}| \ll 1/|\mathbf{q}|$ implies that the electron group must be small. However, owing to Coulomb interactions between electrons, this condition prevents a high radiation output.

The second option involves using periodical ρ_e and/or ρ_{ℓ}. For example, taking ρ_{ℓ} as a constant and ρ_e as periodical,

$$\rho_e(z) = \sum_{n=1}^{N_e} \delta(z - na), \tag{29}$$

where a is the periodic spacing and N_e denotes the total number of electron bunches. The corresponding form factor is given by:

$$F(q_z) \propto \sum_{n=1}^{N_e} e^{inaq_z}. \tag{30}$$

Under the Bragg scattering condition, given that $q_z = 2\pi m/a$, the m-th term in the sum constructively interferes. This constructive interference leads to coherent scattering,

$$I_{\ell'} \propto \left|F(q_z)\right|^2 \propto N_e^2. \tag{31}$$

The same conclusion holds true if the photons have a periodic structure, $I_{\ell'} \propto N_{\ell}^2$.

Therefore, coherent Compton scattering involves periodic electron and photon bunches, which are key to achieving high-intensity scattered radiation.

Different light sources use different strategies. For a wiggler, incoherent radiation arises as electrons pass through a magnetic structure, with an output light intensity scaling of [23]: $I \propto N_e \cdot N_B$, where N_B denotes the number of photon (or virtual photon) periods. In the case of an undulator, because of the periodicity of the magnets, the intensity scales are $I \propto N_e \cdot N_B^2$. In the case of FELs, microbunches of electrons can result in intensity scaling, as follows: $I \propto N_e^2 \cdot N_B^2$.

Coherent Compton scattering is an example of a quantum coherence-enhanced phenomenon. As a special case of Compton scattering, coherent Compton scattering has been widely studied in various experimental and astrophysical contexts [24]. For example, astronomical observations are believed to be manifestations of coherent Compton scattering of light on well-structured charge layers surrounding celestial bodies [25, 26]. Coherent Compton scattering in van der Waals materials has also been observed experimentally [27]. Additionally, the Kapitsa–Dirac effect is often interpreted as a special case of coherent Compton scattering, in which electrons are scattered by periodical photons [28]. Coherent Compton scattering, involving low-energy electrons interacting with standing waves, has been experimentally observed [29]. Similar to other quantum coherence phenomena, coherent Compton scattering follows the characteristic scaling laws of $I \propto N_B^2$, and $I \propto N_e^2$. The scaling laws can be used to generate high-intensity photon beams.

4 Coherent Compton light source with sOAP

The proposed setup is shown in Fig. 3. An incident plane-wave laser pulse first passes through an optical diffractive grating element, where α represents the tilt angle between the pulse front and phase front. While the phase front remains perpendicular to the propagation direction [30–32], the laser arrival time is delayed in proportion to the radius of the parent stretched parabola, expressed as $\Delta t_1 = r\tan\alpha/c$. When $\alpha \to 0$, $\Delta t_1 \simeq r\alpha/c$.

Next, the front-tilted pulse is focused using the sOAP. Due to the time delay Δt_1, Eq. 20 becomes:

$$\frac{\mathrm{d}(AC - z + r\alpha)}{\mathrm{d}f} = \frac{\alpha + \frac{r\eta}{f_0} - \frac{r^3\eta}{4f_0^3}}{\frac{r\eta}{f_0} + \frac{r^3\eta}{4f_0^3}}. \tag{32}$$

The corresponding speed of focus is given by:

$$v_f = \frac{1 + z/f_0}{1 - z/f_0 + \alpha f_0/\eta r}c. \tag{33}$$

From this equation, it is evident that, by selecting an appropriate tilt angle α, v_f can be made smaller than c, unlike the case described in Eq. 21. By setting $v_f = \beta c$ to match

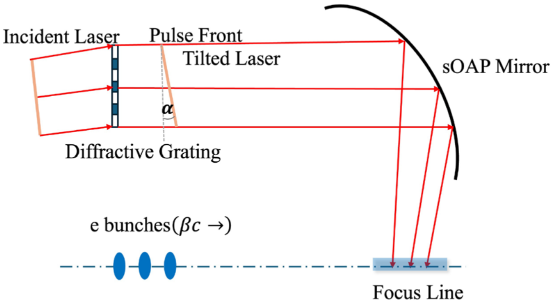

Fig. 3 (Color online) Proposed setup for coherent Compton scattering: An incident plane-wave laser is tuned by a diffractive optical part such as grating or a prism [30, 31] and then transformed into a tilted pulse laser. This tilted pulse is then focused by a sOAP mirror. A train of electron bunches interplay with the resulting focal line, producing high-intensity coherent Compton scattering

the electron speed, the interaction between electrons and photons can be sustained for an extended duration. This is crucial for achieving highly coherent interactions.

Accordingly, the phase variations in Eq. 22 can be modified as follows:

$$\frac{\mathrm{d}\phi}{\mathrm{d}f} = \frac{2\pi}{\lambda}\frac{1 - z/f_0 + \alpha f_0/\eta r}{1 + z/f_0}. \tag{34}$$

The focal length of the combined setup remains the same as that before, as shown in Eq. 25.

To maintain coherent scattering, the electron bunch length must be significantly shorter than the incoming radiation wavelength, allowing all electrons to radiate in phase. Achieving this in the optical laser range is challenging, because typical electron pulses are larger than several millimeters. The concept of SSMB has been proposed to address this issue. However, owing to Coulomb expansion, it is difficult to achieve a small bunch that contains many electrons.

As shown in Refs. [21, 22], electron-beam scattering with a laser beam at a 90° angle always produces coherent radiation. This is because only a small slice of electrons interact with the photons at this interaction angle. Within this slice, all electrons interact coherently.

At a 90° angle, with a single focal point, the enhancement factor is [22],

$$\mathcal{R}(\theta_L \approx 0) \propto \frac{N_\mathrm{e}}{4\pi}\frac{(\lambda_\mathrm{s}/\gamma^2)}{\sigma_{z,L}}e^{-4\tilde{q}^2}, \tag{35}$$

where N_e denotes the number of electrons, λ_s is the wavelength of the scattered photons, γ is the relativistic factor of the electrons, $\sigma_{z,L}$ is the cross section of the laser along the z-direction, and $\tilde{q}$ is a geometric factor [21, 22].

At the 90° angle, where $z \simeq f_0$, Eq. 34 becomes:

$$\frac{\mathrm{d}\phi}{\mathrm{d}f} \simeq \frac{2\pi}{\lambda}\frac{\alpha f_0}{2\eta r} \simeq \frac{2\pi}{\lambda}\frac{\alpha}{4\eta}, \tag{36}$$

and Eq. 33 becomes:

$$v_\mathrm{f} = \frac{4\eta}{\alpha}c. \tag{37}$$

Considering this, as shown in Eq. 28, the coherence scales as $I_{\ell'} \propto N_\mathrm{e}^2 N_\ell^2$ whereas the incoherent scattering scales as $I_{\ell'} \propto N_\mathrm{e} N_\ell$. Thus, coherent approaches have the potential to surpass incoherent approaches, such as the current basis of LPP, in the long run. For an extended focus volume, based on Eq. 28, the enhancement factor (Eq. 35) is further amplified to obtain:

$$\mathcal{R}(\theta_L \approx 0) \propto \frac{N_\mathrm{e} N_l}{4\pi}\frac{\lambda_\mathrm{s}/\gamma^2}{\sigma_{z,L}}e^{-4\tilde{q}^2}, \tag{38}$$

where N_l denotes the number of photons in the laser. Due to the large enhancement factor $N_\mathrm{e}N_l$, a high-intensity and highly coherent scattered photon beam can be achieved. Numerical estimations are presented in Table 1. A train of electron bunches with the same initial velocity (SSMB) [7], successively collides with the laser reflected by the sOAP mirror, which causes inverse Compton scattering. A coherent photon beam with a flux of 10^{16} photons/s appears promising, given the capabilities of current laser technologies.

The coherence of the scattering is determined by the double form factor (Eq. 27), which is an integral highly dependent on the laser wavelength (λ). To ensure coherence in the sOAP setup, the tolerances of the optical components, including the sOAP mirror and wavefront tilt element, as well as the precision of the optical alignment, should be on the order of λ or smaller to achieve a higher coherent effect. Additionally, the stability of both the electron and laser beams should be maintained on the order of λ (or for a time δt on the order of λ/c) to ensure that the two beams collide at the right spot and at the right time. Compared with other EUV generation methods, this is a trade-off. However, with modern technologies, sub-µm (spatial) and sub-ps (temporal) precisions can be achieved, making electron laser matching, including alignment and stability, feasible.

Table 1 Example of coherent scattering with the sOAP at 90°

Electron bunches	
Number of electrons	$N = 3 \times 10^{10}$ (4.8 nC)
Electron energy	$E = 3.2\,\mathrm{MeV}$ ($\gamma = 6.26$)
Bunch length (LAB)	$L_z = 1\,\mathrm{mm}$ (10 ps)
Laser pulse (CO$_2$)	
Wavelength	$\lambda = 10.6\,\mu\mathrm{m}$
Power/pulse length	$W = 12\,\mathrm{J}/3\,\mathrm{ps}$
Repetition rate	$f = 1\,\mathrm{kHz}$
sOAP	
Focus	$f_0 = 10\,\mathrm{cm}$
Deformation parameter	$\eta = 0.01$
Reflection angle range	$85° < \theta < 90°$
Tilt angle	$\alpha = 10°$
Scattered photons	
EUV energy	92 eV, or 14 nm
Laser and beam spot size	5 µm
Central cone aperture	$\Delta\theta_\mathrm{L} \simeq 10°$
Coherent enhancement factor	$\mathcal{R} \simeq 10^4$
Scattered photon number	$N_\mathrm{coh} \simeq 1.1 \times 10^{16}/\mathrm{s}$

5 Summary

EUV lithography is critical for the semiconductor industry. However, the current tin-droplet-based light sources used in lithography face numerous limitations, highlighting the urgent need for next-generation technology.

In this study, the application of a sOAP was proposed to generate a coherent Compton light source. A flying focus train of photons can be created by combining a sOAP with a tilted pulse laser. When this highly periodic photon train, structured both temporally and spatially, interacts with highly periodic electron bunches, enhanced coherent EUV radiation can be generated. It is estimated that, by leveraging existing CO_2 lasers in conjunction with a sOAP, it is possible to achieve a flux of 10^{16} photons per second at a wavelength of 14 nm. The proposed method, with its distinct advantages, holds significant promise as the foundation for next-generation EUV light sources.

Furthermore, the demand for high-quality light sources for fundamental scientific research and industrial applications is increasing rapidly. This includes the pursuit of extreme performance across multiple dimensions, such as a higher resolution (energy, spatial, and angular resolution), broader spectral range, and higher light intensity for applications in laser processing, optical communication, medical imaging, and fundamental research.

Taking advantage of the electrons coherently interacting with a moving photon focus spot, the coherent scattering from the sOAP setup is not limited to the EUV band. They can also be used to generate other wavelengths, including soft X-rays and X-rays, by increasing the electron energy or adjusting the laser wavelength. Furthermore, the proposed scheme is significantly more compact than devices such as FELs or synchrotron radiation facilities, potentially revolutionizing soft X-ray and X-ray applications in large-scale research infrastructures.

Author contributions All authors contributed to the study. The conception and design were led by Chang-Bo Fu. Material preparation and data analysis were carried out by Kai Zhao and Chang-Bo Fu. Editing and review were undertaken by Chang-Bo Fu and Yu-Gang Ma. In addition, Yu-Gang Ma was responsible for providing resources and supervision. The first draft of the manuscript was written by Kai Zhao and Chang-Bo Fu, and all authors commented on previous versions of the manuscript. All authors read and approved the final version of the manuscript.

Data availability The data that support the findings of this study are available from the corresponding author upon reasonable request.

Declarations

Conflict of interest Yu-Gang Ma is the editor-in-chief for Nuclear Science and Techniques and was not involved in the editorial review, or the decision to publish this article. All authors declare that there are no conflict of interest.

References

1. V. Bakshi, *EUV Lithography*, 2nd edn. (SPIE Press, Bellingham Washington, 2018)
2. N. Fu, Y.X. Liu, X.L. Ma et al., EUV lithography: state-of-the-art review. J. Microelectron. Manuf. **2**, 19020202 (2019). https://doi.org/10.33079/jomm.19020202
3. H.J. Levinson, High-NA EUV lithography: current status and outlook for the future. Jpn. J. Appl. Phys. **61**, SD0803 (2022). https://doi.org/10.35848/1347-4065/ac49fa
4. D. Kazazis, J.G. Santaclara, J. van Schoot et al., Extreme ultraviolet lithography. Nat. Rev. Methods Primers **4**, 84 (2024). https://doi.org/10.1038/s43586-024-00361-z
5. D.K. Yang, D. Wang, Q.S. Huang et al., The development of laser-produced plasma EUV light source. Chip **1**, 100019 (2022). https://doi.org/10.1016/j.chip.2022.100019
6. N. Nakamura, R. Kato, H. Sakai et al., EUV-FEL light source for future lithography. In: Paper Presented at the 14th International Particle Accelerator Conference (Venice, Italy, IPAC2023: THPM123, 2023)
7. X.J. Deng, A. Chao, J. Feikes et al., Experimental demonstration of the mechanism of steady-state microbunching. Nature **590**, 576–579 (2021). https://doi.org/10.1038/s41586-021-03203-0
8. J.H. Ko, M.W. Kim, S. Lee et al., Strip-line injection kicker for PAL-EUV booster synchrotron. J. Korean Phys. Soc. **84**, 189–197 (2024). https://doi.org/10.1007/s40042-023-00997-2
9. N. Nakamura, R. Kato, H. Sakai et al., High-power EUV free-electron laser for future lithography. Jpn. J. Appl. Phys. **62**, SG0809 (2023). https://doi.org/10.35848/1347-4065/acc18c
10. H.P. Freund, T.M. Antonsen, *Principles of Free-Electron Lasers*, 4th edn. (Springer, Switzerland, 2024)
11. D. Ramsey, B. Malaca, T.T. Simpson et al., X-ray free-electron lasing in a flying-focus undulator (2024). arXiv: 2410.12975
12. D. Turnbull, S.W. Bahk, I.A. Begishev et al., Flying focus and its application to plasma-based laser amplifiers. Plasma Phys. Control. Fusion **61**, 014022 (2019). https://doi.org/10.1088/1361-6587/aada63
13. D.H. Froula, J.P. Palastro, D. Turnbull et al., Flying focus: Spatial and temporal control of intensity for laser-based applications. Phys. Plasmas **26**, 032109 (2019). https://doi.org/10.1063/1.5086308
14. M.V. Ambat, J.L. Shaw, J.J. Pigeon et al., Programmable-trajectory ultrafast flying focus pulses. Opt. Express **31**, 31354–31368 (2023). https://doi.org/10.1364/OE.499839
15. D.H. Froula, D. Turnbull, A.S. Davies et al., Spatiotemporal control of laser intensity. Nat. Photon. **12**, 262–265 (2018). https://doi.org/10.1038/s41566-018-0121-8
16. T.T. Simpson, D. Ramsey, P. Franke et al., Spatiotemporal control of laser intensity through cross-phase modulation. Opt. Express **30**, 9878–9891 (2022). https://doi.org/10.1364/OE.451123
17. S. Smartsev, C. Caizergues, K. Oubrerie et al., Axiparabola: a long-focal-depth, high-resolution mirror for broadband high-intensity lasers. Opt. Lett. **44**, 3414–3417 (2019). https://doi.org/10.1364/OL.44.003414
18. K. Oubrerie, I.A. Andriyash, R. Lahaye et al., Axiparabola: a new tool for high-intensity optics. J. Opt. **24**, 045503 (2022). https://doi.org/10.1088/2040-8986/ac57d2
19. J.J. Pigeon, P. Franke, M.L.P. Chong et al., Ultrabroadband flying-focus using an axiparabola-echelon pair. Opt. Express **32**, 576–585 (2024). https://doi.org/10.1364/OE.506112
20. A. Liberman, R. Lahaye, S. Smartsev et al., Use of spatiotemporal couplings and an axiparabola to control the velocity of peak intensity. Opt. Lett. **49**, 814–817 (2024)

21. A. Luccio, L. Miceli, Coherent Compton x-ray sources. J. X-ray Sci. Technol. **4**, 247–262 (1994). https://doi.org/10.1016/S0895-3996(05)80043-6
22. G. Giordano, G. Matone, A. Luccio et al., Coherence in Compton scattering at large angles1. Laser Particle Beams **15**, 167–177 (1997). https://doi.org/10.1017/S0263034600010867
23. W.Q. Hua, C.M. Yang, P. Zhou et al., Time resolved ultra small angle X ray scattering beamline (BL10U1) at SSRF. Nucl. Sci. Tech. **35**, 36 (2024). https://doi.org/10.1007/s41365-024-01389-2
24. L.X. Liu, H.W. Wang, G.T. Fan et al., The SLEGS beamline of SSRF. Nucl. Sci. Tech. **35**, 111 (2024). https://doi.org/10.1007/s41365-024-01469-3
25. B. Zhang, Coherent inverse Compton scattering by bunches in fast radio bursts. Astrophys. J. **925**, 53 (2022). https://doi.org/10.3847/1538-4357/ac3979
26. B.D. Metzger, B. Margalit, L. Sironi, Fast radio bursts as synchrotron maser emission from decelerating relativistic blast waves. Mon. Notices R. Astron. Soc. **485**, 4091–4106 (2019). https://doi.org/10.1093/mnras/stz700
27. M. Shentcis, A.K. Budniak, X.H. Shi et al., Tunable free-electron X-ray radiation from van der Waals materials. Nat. Photon. **14**, 686–692 (2020). https://doi.org/10.1038/s41566-020-0689-7
28. H. Batelaan, Colloquium: illuminating the Kapitza-Dirac effect with electron matter optics. Rev. Mod. Phys. **79**, 929–941 (2007). https://doi.org/10.1103/RevModPhys.79.929
29. K. Lin, S. Eckart, H. Liang et al., Ultrafast Kapitza-Dirac effect. Science **383**, 1467–1470 (2024). https://doi.org/10.1126/science.adn1555
30. P. Baum, A.H. Zewail, Breaking resolution limits in ultrafast electron diffraction and microscopy. Proc. Natl. Acad. Sci. U.S.A. **103**, 16105–16110 (2006). https://doi.org/10.1073/pnas.0607451103
31. J. Hebling, Derivation of the pulse front tilt caused by angular dispersion. Opt. Quantum Electron. **28**, 1759–1763 (1996). https://doi.org/10.1007/BF00698541
32. C. Chang, C.X. Tang, J.H. Wu, High-gain Thompson-scattering X-ray free-electron laser by time-synchronic laterally tilted optical wave. Phys. Rev. Lett. **110**, 064802 (2013). https://doi.org/10.1103/PhysRevLett.110.064802